Electronic Supplementary Information

A Compact and High-Performance Setup of Capillary Electrophoresis with Capacitively Coupled Contactless Conductivity Detection (CE-C^4D)

Lin Li,[§] Yun-Peng Song,[§] Dou-Dou Ren, Tang-Xiu Li, Ming-Hui Gao, Lei Zhou, Zhi-Cong Zeng*

and Qiaosheng Pu*

State Key Laboratory of Applied Organic Chemistry, College of Chemistry and Chemical Engineering, Lanzhou University, Lanzhou 730000, China

[§]These authors contributed equally to this work.

*Corresponding Author. Email: zengzc@lzu.edu.cn; puqs@lzu.edu.cn.

Table of Contents:

Statement: This work is a continuation of our previous work (Pushing the Limits of Capillary Electrophoresis with Capacitively Coupled Contactless Conductivity Detection (CE-C^4D)), which is currently under review. For a better understanding of this work, we present the contents of Section 4−Section 9, Section 11 and Section 12 in this ESI.

1. High-voltage power supply (HVPS)

CE requires the use of a high-voltage power supply (HVPS) for separation and electrokinetic injection; a reliable HVPS ensures the reproducibility of the separations, the migration times and the peak areas. Commercial HVPS are user-friendly and ready-to-use but bulky and somewhat expensive, making them unsuitable for portable instruments; while some small-sized and less expensive HVPS modules lack useful functions, such as voltage ramping control. Here, we tried to build a miniaturized HVPS by ourselves. The design principle of the HVPS circuit was shown in Figure S1A. For simplicity, decoupling capacitors at the ICs were not shown. The main features of this HVPS included: 1) 0 to 25 kV output voltage; 2) 0 to 300 μA output current; 3) with monitors of output voltage and current; 4) output voltage regulation; 5) with output current limiting protection circuit; 6) easy conversion to negative output (0 to -25 kV, polarity switching) just by connecting the voltage multiplier circuit in reverse (Figure S2). The boosted circuit (green area) contained: NE555 chip, MOSFET, transformer and voltage multiplier circuit (pairs of diode−capacitor, each withstand voltage 15 kV); the NE555 output a pulse-width-modulation (PWM) waveform to turn on and off the MOSFET. The designed PWM frequency was approximately 40 kHz, which automatically adjusted as the feedback progressed. The AC output voltage of the transformer was converted to DC and multiplied by the voltage multiplier circuit (4 or 5-stage). The control circuit (blue area) contained: the output of the HVPS was attenuated by R_2 (high-voltage (HV) resistor, withstand voltage 30 kV) and R_3 resistors (2500:1) and used as a feedback signal; the signal was normalized (U_5) and then sent to the rectifier circuit (U_6); then the signal was sent to U_8 for voltage monitor, or sent to U_7 of proportional-integral (PI) feedback and further sent to the control pin of the NE555 to stabilize the output voltage. The limited current circuit (orange area) contained: the current was sensed by R_1 and buffered by U_1; U_2 was a rectifier; U_4 was a current monitor, and U_3 worked like a comparator to turn off the NE555 if the current signal was greater than the setting voltage of Ref1. The real photo was shown in Figure S1B, which contained a low voltage control circuit board and a high-voltage insulating silicone section. Figure S1D showed the response time was about 20 ms. Figure S1E showed the method for output ripple voltage test and its result (inset); the ripple was only 0.05% at 15 kV output. The method for ripple measurement of HVPS has been used in many companies (e.g. Spellman: High Voltage Reference Manual, Section 5, Standard test procedures for high voltage power supplies). Finally, we used 1 μM Li^+ as a sample for comparison, and as shown in Figure S1F, there was no significant difference in performance compared with a commercial HVPS (DW-P303-1CV1, Dong Wen High Voltage, China).

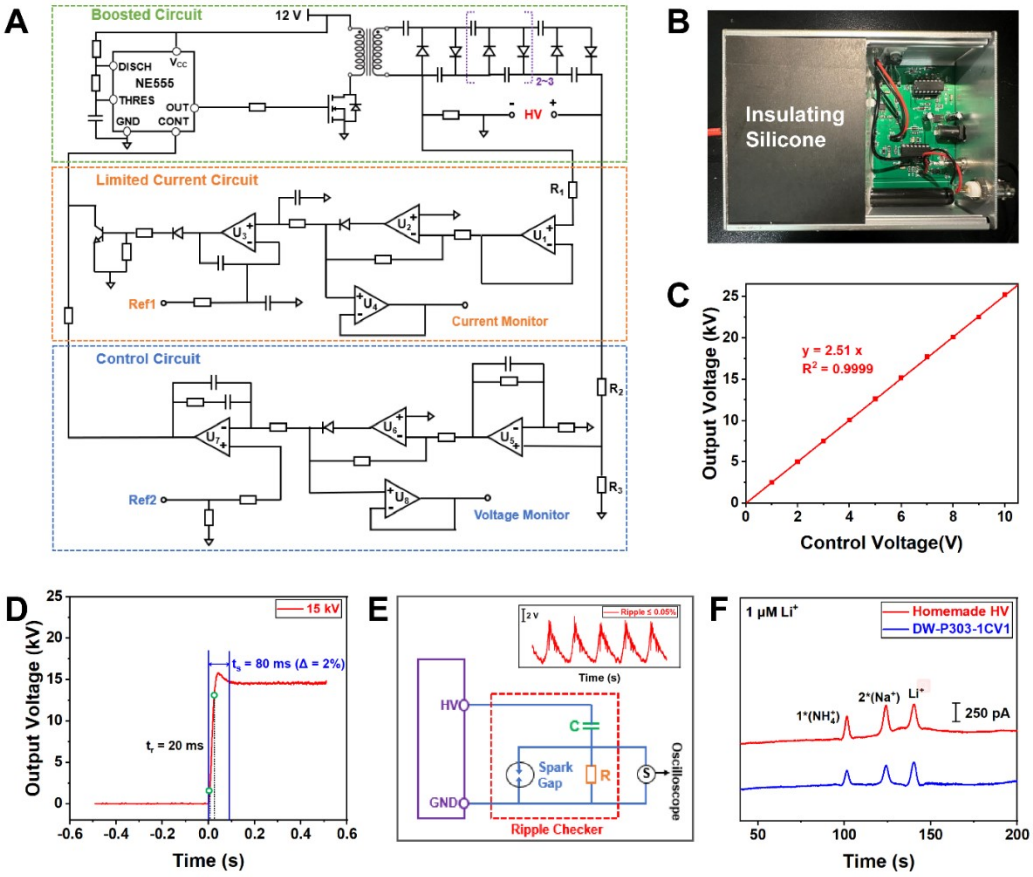

Figure S1. (A) Principle of our HVPS circuit design. (B) Real photo of our HVPS with a size of 13 × 8 × 5 cm^3. The transformer and the voltage multiplier circuit are covered under the insulating silicone. (C) Linearity of the control voltage and the output voltage. (D) Response time test. The rise time (10%–90%) is about 20 ms and the settling time (2% error) is about 80 ms for 15 kV output. (E) Method for output ripple voltage test and its result (inset). Test method: a DC blocking capacitor, C, in series with the HVPS output terminal, is used to pass the AC component in the output voltage directly to the oscilloscope, S. Resistor, R, and spark gap, SG, protect the oscilloscope against surges in the output voltage which can be transferred directly through the blocking capacitor to the scope. The ripple is about 0.05% at 15 kV output with our HVPS. (F) Performance comparison of home-built and commercial HVPS (DW-P303-1CV1). Test sample: 1 μM Li^+; BGE: 20 mM MES-His, pH = 6. Capillary: 75 μm ID, 365 μm OD; 22 cm separation length, and 64 cm total length; hydrodynamic injection: 40 s at 10 cm height; separation voltage: +15 kV; 1 MHz sine wave with an effective excitation voltage of 40 V_{pp}. *—system peak, due to the residual NH_4^+ and Na^+.

2. Construction of negative HVPS

Figure S2A is a positive voltage multiplier circuit. Just reverse the directions of all the diodes in it to convert it into a negative voltage multiplier circuit (Figure S2B), thereby realizing the construction of a negative HVPS. It is worth noting that U_2 and U_6 are absolute value circuits, which ensures easy polarity conversion of this HVPS. As shown in Figure S2C, for the negative input ($V_{IN} < 0$), diode D_1 is forward biased and the circuit operates as a conventional inverter with a gain of -1 ($R_1 = R_2$), therefore, $V_{OUT} = -V_{IN} = |V_{IN}|$. For the positive input ($V_{IN} > 0$), diode D_1 is reverse biased disconnecting the output from the amplifier. The output will be at the virtual ground potential (- input terminal) through resistor R_2, therefore, $V_{OUT} = V_{IN} = |V_{IN}|$.

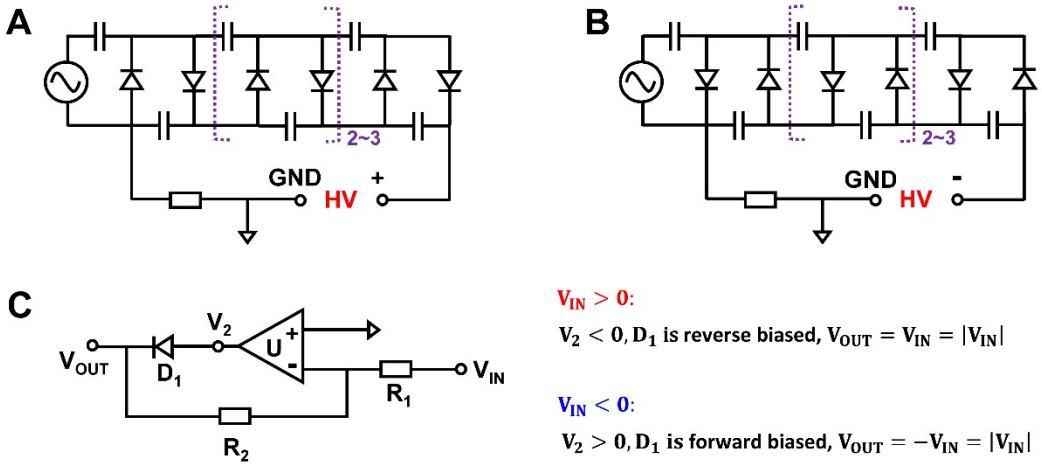

Figure S2. (A) Schematic diagram of positive voltage multiplier circuit. (B) Schematic diagram of negative voltage multiplier circuit. (C) Principle of absolute value circuit.

3. DDS Function Generator

In fact, one of the difficulties in the miniaturization of the C^{4}D detector is to reduce the size of the function generator. There have been reports on integrated function generator designs, such as LC oscillator circuit with a transistor[1], XR-2206[2], MAX038[3], NE555[4], a triangle-wave oscillator[5]. However, some older chips (XR-2206 and MAX038) have been no longer produced. In addition, the fixed frequency and amplitude are the main drawbacks, not as convenient as commercial function generators. Here, we used the direct digital synthesis (DDS) technique to reduce the size of the function generator. It could also provide the functions of adjustable output amplitude, selectable excitation frequency and sweeping frequency. There are many advantages of the DDS technique, such as stable frequency output, digital frequency tuning, fast tuning response time, high spectral purity, low power consumption and cost effectiveness. The AD9834 is a 75 MHz low power DDS device capable of producing high-performance sinusoidal and triangular outputs (Figure S3A), which can achieve a frequency tuning resolution of 0.28 Hz. However, the output amplitude of AD9834 is only 0.6 V_{pp}, and the amplitude follows a SINC(x) roll-off response, which means the amplitude decreases significantly at higher frequencies (Figure S3C). In order to solve this problem, we used a 1/SINC(x) filter (OP1, R_2, R_1, C_2) to counteract the effect of SINC(x) roll-off (Figure S3B), but the real performance of the filter alone was not good enough (Figure S3D, red curve), because the values of the resistors or the capacitor were not continuously, which resulted in the real value used couldn't match well with the design. We also noticed the amplitude of the output waveform could be modulated by adjusting the current through FS ADJUST pin of the AD9834; more details of this method could be found in the circuit note of CN0156 from Analog Devices company; here we used the 12-bit DAC (V_{DAC}) of the teensy 3.2 MCU to drive the FS ADJUST pin of the AD9834 through a series resistor. A flat output amplitude was achieved shown in Figure S3D (green curve). Then the output amplitude was further amplified by using a wide bandwidth operational amplifier (OP2) with a gain of R_4/R_3. Finally, we could obtain a flat amplitude of about 19.6 V_{pp} up to 2 MHz. Besides the amplitude compensation, the output amplitude of the DDS (e.g., from 1V to 20V) could also be adjusted by software programming the current in the FS ADJUST pin of the AD9834. The optimized DDS strategy made the custom-made DDS function generator suitable for routine CE-C^{4}D experiments (Figure S3E).

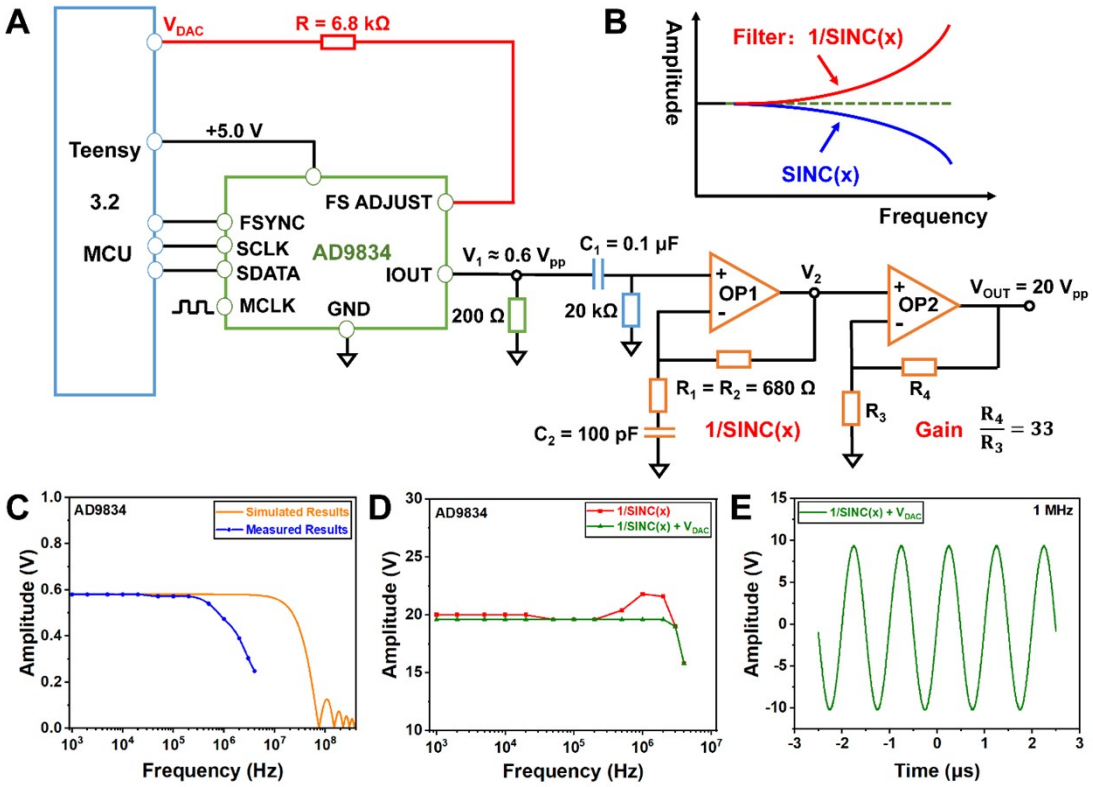

Figure S3. DDS function generator. (A) Electronic diagram of the design. The AD9834 is controlled by Teensy 3.2 MCU; OP1 combined with R_2, R_1, C_2 is used as a 1/SINC(x) filter; OP2 combined with R_4, R_3 is used as a gain amplifier. (B) Scheme of 1/SINC(x) filter to eliminate the effect of SINC(x) roll-off. (C) The output amplitude roll-off with frequency. (D) Amplitude compensation. Test with 1/SINC(x) filter only (red curve); test with 1/SINC(x) filter and V_{DAC} (green curve). (E) Final output amplitude of the DDS function generator; test at 1 MHz, 19.6 V_{pp}.

4. Schematic diagram of our differential CE-C^{4}D setup.

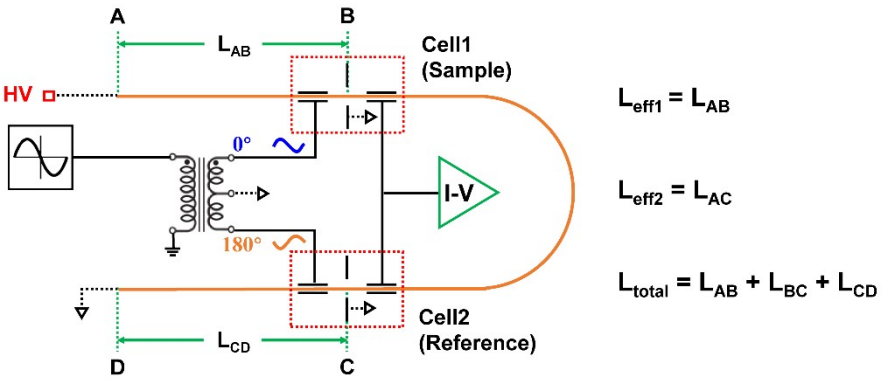

Figure S4. Schematic diagram of our differential CE-C^{4}D setup by a single capillary.

In this work, a single capillary was used by looping the end of the separation capillary back through the reference part of the cell (Figure S4). When using a differential C^{4}D cell, either a single capillary or two capillaries can be used; however, the single capillary configuration shows better suppression of baseline drift, which is critical for trace analysis. This configuration is nearly the same as the one previously published by

Prof. Hause's group[6]. However, with the "effective" differential detection and low noise circuit system, the sensitivity has a great improvement (about 25 times). There were two effective lengths (L_{eff1} and L_{eff2}). As the ions traveled through the detector twice, duplicate peaks with opposite sign were obtained. The two effective lengths (L_{eff1} and L_{eff2}) and the total lengths (L_{total}) of the capillary need to be optimized to avoid any overlap of peaks from the first and second passage. Due to the peak broadening and longer time for the second passage, we mostly used the signal of the first passage in this work unless otherwise specified.

5. Details of the "effective" differential detection

One limitation of the sensitivity improvement for CE-C^4D is the strong background signal (or current) of BGE, as the concentration of BGE (e.g. 20 mM) is much higher than detected signal ions (only several nM to μM). For the CE-C^4D detection, the signal comes from the difference between the BGE and the measured ions, and high background signal of BGE is accompanied by high noise[6]. However, in suppressed ion chromatography (IC), as we know, the suppressor plays a central role, which has the dual functions of reducing the background of BGE and increasing the detected ion signal[7, 8]. However, this method cannot be directly transferred to CE. Differential detection should be a good method to suppress the high conductivity background signal of the BGE, which has been widely used in optical detection[9, 10] and could detect small signal changes such as 10^{-7} (e.g. 1 μV signal change in a 10 V baseline). Several types of differential detection have been used in previous CE-C^4D literature[6, 11–17]. However, there were no significant sensitivity improvements being observed, which may further indicate the complexity of the problem.

In order to perform "effective" differential detection, we believe that two key factors must be met: 1) carefully adjust the two C^4D cells and reduce the BGE signal to below 3% of the initial value of a single C^4D cell; 2) increase the ion signal and enable lower the noise levels of the detection system, e.g., the signal of the 20 nM ion should be 3× better than the noise of the entire system. In this work, a custom-made transformer was fabricated with a toroidal high frequency ferrite core, which has two outputs with exact inverse phase (0° and 180° phase) at 1 MHz; and the two C^4D cells were adjustable. Due to the combination of in-depth C^4D model study, low noise I-V converter design and lock-in (or RMS-to-DC) detection, the electronic noise of our I-V converter is about 0.5 μV, which only accounts for a minor part of the total noise in our CE-C^4D system. In our case, we were able to extract the weak ion signals as low as 10^{-6} (e.g. 10 μV signal change in a 10 V baseline) from the BGE, and we found that "effective" differential detection and good signal conditioning circuitry were quite important to achieve extremely low noise levels.

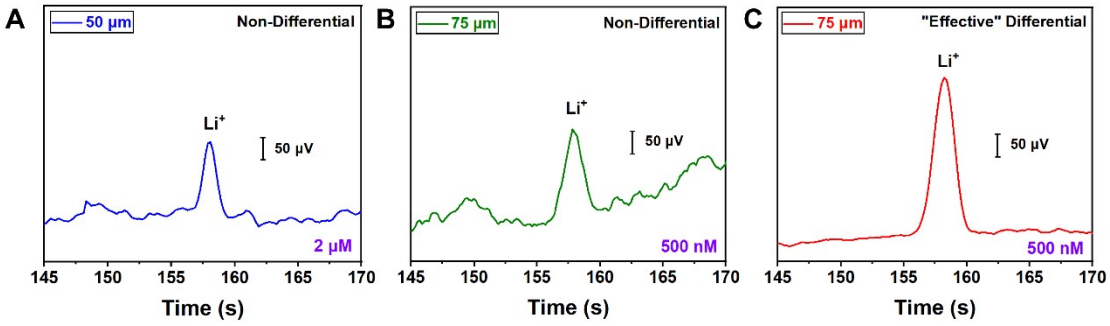

Figure S5. Differential effect evaluation of the newly developed CE-C^4D. (A) Electropherogram of 2 μM Li^+, non-differential detection; capillary with 50 μm ID and 365 μm OD, 1 MHz sine wave with an effective excitation voltage of 20 V_{pp}. (B) Electropherogram of 500 nM Li^+, non-differential detection; capillary with 75 μm ID and 365 μm OD, 1 MHz sine wave with an effective excitation voltage of 20 V_{pp}. (C) Electropherogram of 500 nM Li^+,

"effective" differential detection; capillary with 75 µm ID and 365 µm OD, 1 MHz sine wave with an effective excitation voltage of 40 V_{pp}. Other electrophoretic conditions are the same: BGE: 20 mM MES-His, pH = 6; separation voltage, +15 kV; capillary effective length: 20 cm, total length: 64 cm; hydrostatic injection: 40 s at 10 cm height.

The comparison between non-differential and "effective" differential of our developed setup is shown in Figure S5). When the non-differential detection is used, we can see significant noise and baseline drift from Figure S5A and Figure S5B. To avoid signal saturation due to the background signal of BGE, we cannot use higher excitation voltages, which will limit the detection limit of the setup. For the capillary ID increases from 50 µm to 75 µm, we found the signal for the same concentration of Li^+ increases by about 4-5 times but the noise increases about 2 times, and the S/N ratio increases only by about 2 times. Therefore, using a 50 µm capillary to test 2 µM Li^+ (Figure S5A) and using a 75 µm capillary to test 500 nM Li^+ (Figure S5B) have similar signal-to-noise ratios. 2) When the "effective" differential detection is used, we can see that the noise (reduced by about 10 times) and baseline drift are significantly decreased from Figure S5C. It is worth noting that the "effective" differential detection allows the use of a higher excitation voltage and a larger inner diameter capillary (ID = 75 µm) to increase the ion signal while reducing the noise. The results show that the "effective" differential detection can improve the S/N ratio by 20 to 40 times, which ensures that our setup has the detection sensitivity of trace analysis.

6. Design of the high-performance I-V converter

The figure used here just for illustration. The Bode plot helps determine the circuit's stability, bandwidth and noise. Figure S6A shows the noise analysis of the I-V converter that uses a TIA circuit. There are three main sources of noise in the high gain and high bandwidth TIA circuit: feedback resistor noise (E_{R_F}), current noise ($E_{N,i}$), and voltage noise ($E_{N,e}$) of noise gain (NG):

$$E_{N,total} = \sqrt{{E_{R_F}}^2 + {E_{N,i}}^2 + {E_{N,e}}^2} = \sqrt{4kTR_F + (i_{N,op}R_F)^2 + \left[(1 + 2\pi FC_S R_F)e_{N,op}\right]^2} \#(1)$$

where k is Boltzmann's constant, T is the temperature, $i_{N,op}$ is input current noise density of the op-amp, F is the band-limiting frequency, and $e_{N,op}$ is the input voltage noise density of the operational amplifier (op-amp). One thing to note is that all these sources are eventually rolled off by the decreasing loop gain of the op-amp, which means, high frequency regions exceeding the band-limiting frequency cannot be fitted with Equation 1.

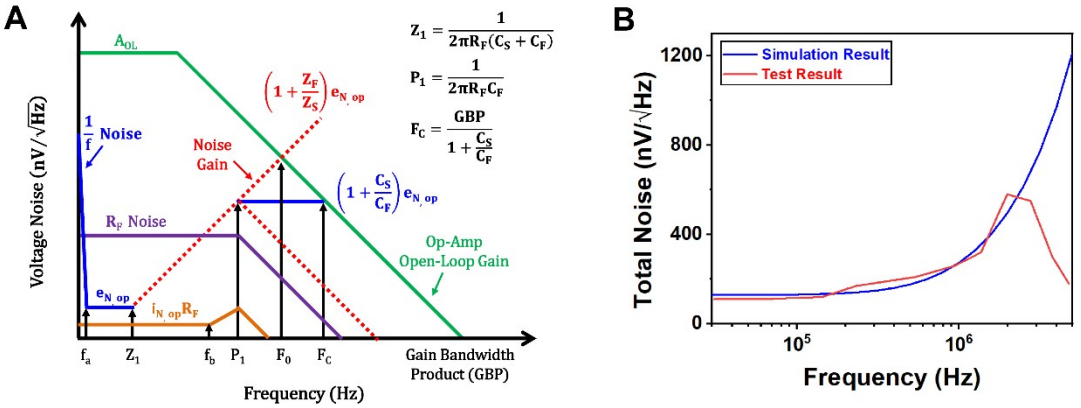

Figure S6. (A) Bode plot magnitude of the I-V converter; (B) Total voltage noise spectral density.

Good noise analysis is important for TIA design. The thermal noise for a 1 MΩ resistor is about 130 nV/Hz$^{1/2}$. With a special design, our I-V converter achieved 4 MHz bandwidth and 300 nV/Hz$^{1/2}$ (at 1 MHz) noise even with a 1 MΩ high-gain resistor. The noise measurement result of I-V converter was shown in Figure S6B, when frequency is less than 2 MHz, the measured output noise of our I-V converter matches the simulated output noise very closely. When $F \leq 100\ kHz$, E_{R_F} dominates. However, as frequency increases, the noise gain increases, and the $E_{N,e}$ also increases and becomes dominant.

7. Separation efficiency of different injection volumes

In order to obtain high sensitivity while maintaining separation efficiency, it is important to select a suitable injection volume. Figure S7 shows the changes in peak height and width of Li^+ under different injection volumes. For a capillary tube with a total length of 64 cm and an ID of 75 μm, with a fixed injection height of 10 cm, the peak height of Li^+ increases linearly when the injection time increases from 8 s to 40 s (Figure S7B). There is also no significant broadening of the peaks (Figure S7A). The injection volume of the sample (V_{inj}) is a function of the capillary length (L) and inner diameter (d), the viscosity of the buffer in the capillary (η), the applied pressure (ΔP), and the injection time (t_{inj}). This volume can be calculated using the Hagen-Poiseuille equation:

$$V_{inj} = \frac{\Delta P d^4 \pi t_{inj}}{128 \eta L} = \frac{\Delta P r^4 \pi t_{inj}}{8 \eta L} \#\ (2)$$

For siphoning injection, the pressure differential for use in equation (2) is given as：

$$\Delta P = \rho g \Delta h \#(3)$$

where ρ is the buffer density, g is the standard acceleration of gravity, and Δh is the height differential of the buffer reservoirs. According to Equation 2 and Equation 3, a height difference of 10 cm creates a pressure difference of 9.8 mbar. It can be seen under the conditions of hydrostatic injection for 40 s at 10 cm height in a capillary with 75 μm ID and 64 cm total length, the injection length accounts for 1.8% of the total capillary length, which is less than 2% and is still applicable. Indeed, all the electropherograms used in this work show good separations.

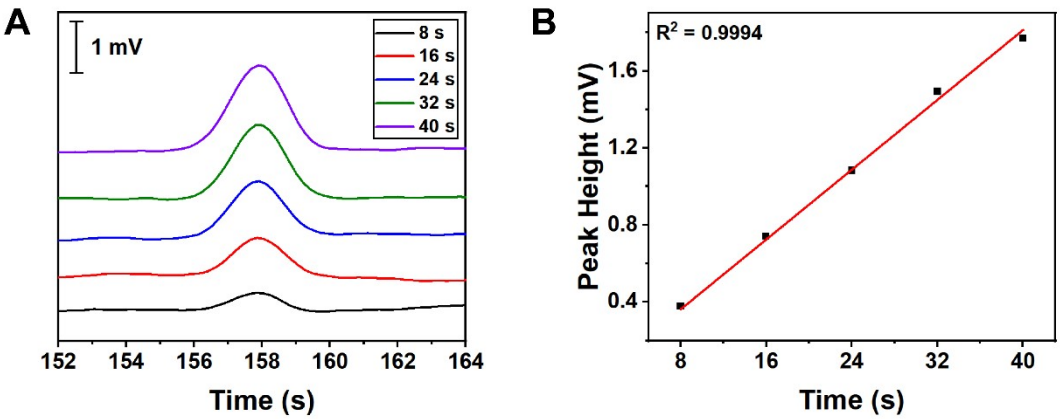

Figure S7. Changes in peak height and width of 5 μM Li^+ under different injection volumes. The injection time of 8 s, 16 s, 24s, 32s and 40 s were tested. Electrophoretic conditions: BGE: 20 mM MES-His, pH = 6; separation voltage: +15 kV; capillary effective length: 20 cm, total length: 64 cm, ID: 75 μm, OD: 365 μm; hydrostatic injection: 10 cm

height; 1 MHz sine wave with an effective excitation voltage of 20 V_{pp}.

8. Effects of 500 nM Li^+ prepared in ultrapure water, tap water and BGE

To assess the stacking effect, we prepared 500 nM Li^+ in ultrapure water, tap water and BGE for further comparison (Figure S8). As a result, 1) when the sample solvent is changed from ultrapure water to BGE (20 mM MES-His, pH = 6), the ion peak height decreases by about 2.5 times, the peak broadens by about 2.1 times, and the signal change is not obvious (Figure S8A and Figure S8C). 2) When the sample solvent is changed from ultrapure water to tap water, as the tap water sample has a normal background conductivity (due to water hardness, ions of Na^+, Ca^{2+}, Mg^{2+}, etc.), it may change the stacking effect. From the results (Figure S8A and Figure S8B), we find that the peak width broadens a bit and the peak height decreases a bit. Notably, the hydrostatic injection method used in this study may be the reason why the effect caused by the stacking effect is not as obvious as that using the electrokinetic injection method (especially for preparing ions in ultrapure water).

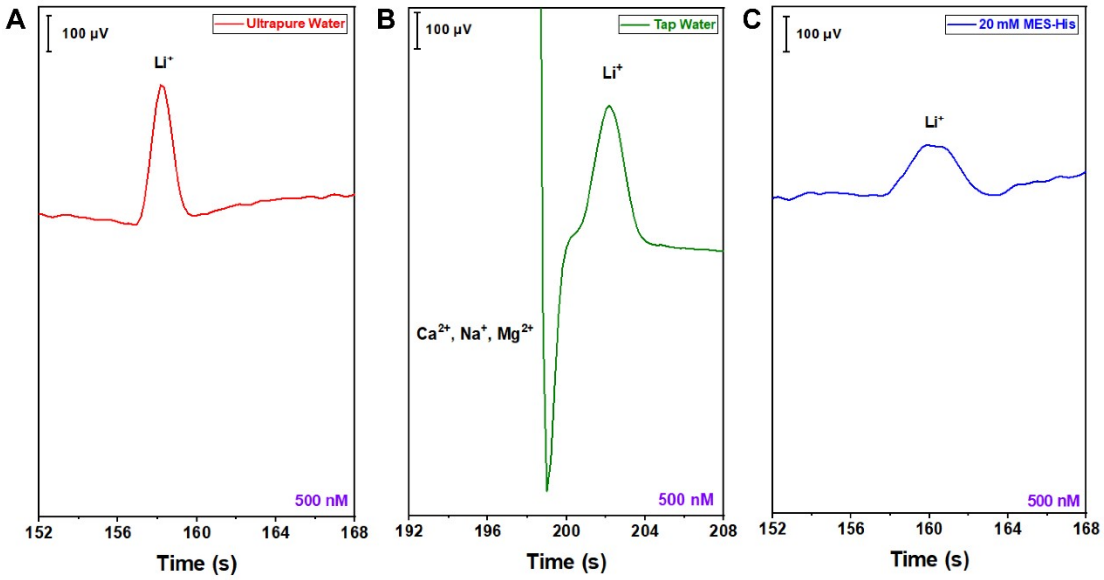

Figure S8. Assessment of the stacking effect. Electropherograms of 500 nM Li^+ in (A) ultrapure water, (B) tap water, and (C) 20 mM MES-His, pH = 6. Electrophoretic conditions: BGE: 20 mM MES-His, pH = 6; separation voltage: +15 kV; capillary effective length: 20 cm; total length: 64 cm, ID: 75 µm, OD: 365 µm; hydrostatic injection: 40 s at 10 cm height; 1 MHz sine wave with an effective excitation voltage of 40 V_{pp}.

9. Separation of the spiked trace heavy metal ions in tap water

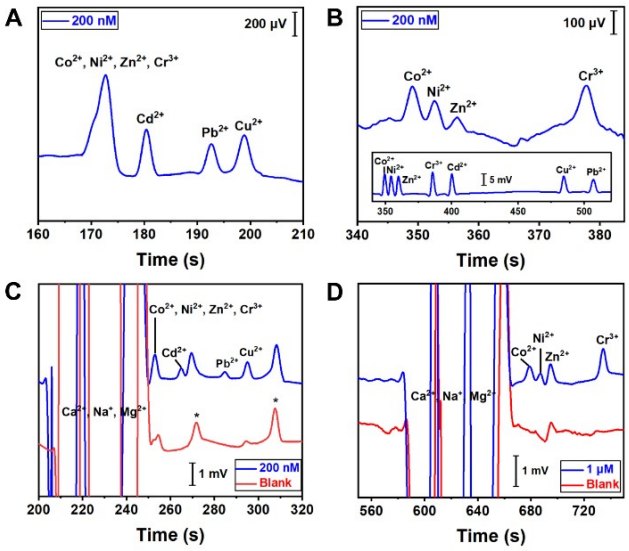

Figure S9. New developed CE-C^{4}D for seven heavy metal ions detection. (A) Electropherogram of 200 nM mixed cations using 1.1 M AcOH as BGE. Capillary effective length: 26 cm, total length: 62 cm. Co^{2+}, Ni^{2+}, Zn^{2+} and Cr^{3+} were not effectively separated. (B) Electropherogram of 200 nM mixed cations using 4.6 M AcOH as BGE. Capillary effective length: 40 cm, total length: 62 cm. Co^{2+}, Ni^{2+}, Zn^{2+} and Cr^{3+} were effectively separated. The inset shows the electropherogram of 20 μM mixed cations using 4.6 M AcOH as BGE. (C) Electropherograms of tap water and the spiked sample with 200 nM mixed cations. BGE: 1.1 M AcOH. Capillary effective length: 31 cm, total length: 75 cm. (D) Electropherograms of tap water and the spiked sample with 200 nM mixed cations. BGE: 4.6 M AcOH. Capillary effective length: 65 cm, total length: 75 cm. Other electrophoretic conditions: separation voltage, +20 kV; capillary with 75 μm ID and 365 μm OD; hydrostatic injection: 40 s at 10 cm height; 1.2 MHz sine wave with an effective excitation voltage of 40 V_{pp}.

10. Real rare-earth mineral analysis

For the sample preparation of the rare-earth mineral: First, to ensure complete dissolution, dissolve 1 g of the pretreated mineral in 5 mL 3 M HCl solution. Second, after the solution cools, add 10 mL of ultrapure water to dilute, and filter with a syringe filter with a pore size of 0.22 μm. Third, transfer 1 mL of the solution to a 100 mL volumetric flask and fill to volume with ultrapure water. According to the electrophoretic results, the calculated contents of various rare-earth elements are shown in Table 1. To verify accuracy of our method, we use the standard addition method for comparison. The spiked sample were prepared by adding equal amounts of elements to the rare-earth mineral sample, and the signals should increase by two times. The results confirmed the accuracy of CE-C^{4}D in analyzing lanthanide elements in the rare-earth mineral sample (Table 1, Figure S10). Since the currently used BGE cannot completely separate Y from Dy, the content of Dy is not shown in the table. In fact, it has been pointed out that in addition to sensitivity, the separation of Eu-Gd, Dy-Y and Yb-Lu remains difficult in the current CE method[18]. Kratii et al. proposed a composition of BGE: 12 mM benzimidazole, 8 mM dipropylglycolic acid, 10 mM glycolic acid, pH = 3.0, which can completely separate 15 rare-earth elements[18]. However, the BGE is suitable for CE-UV, and there are differences between UV and C^{4}D. In addition, dipropylglycolic acid cannot be purchased. Anyway, further development of other better BGEs that can improve the resolution of rare-earth elements is needed.

Table 1. Contents of various rare-earth elements.

Rare-Earth Element	Content (mg/g)		Added (mg/g)	Recovery	
	10 mM HIBA	3 mM HIBA		10 mM HIBA	3 mM HIBA
La	249.4 ± 11.3	238.4 ± 11.0	240	98.6%	99.3%
Ce	10.5 ± 1.7	9.6 ± 1.8	10	97.9%	101.2%
Pr	61.5 ± 5.8	60.2 ± 6.3	61	99.1%	99.3%
Nd	/	254.7 ± 12.9	255	/	99.7%
Sm	44.4 ± 4.1	40.8 ± 4.2	42	100.4%	102.7%
Eu	6.6 ± 0.9	6.1 ± 1.1	6.5	98.3%	101.1%
Gd	31.4 ± 3.6	30.3 ± 3.1	31	101.8%	100.8%
Tb	4.1 ± 1.1	/	4.1	97.1%	/
Dy	/	/	/	/	/
Ho	4.6 ± 1.2	/	4.6	101.1%	/
Er	7.8 ± 1.5	/	7.8	103.7%	/
Tm	1.7 ± 0.3	/	1.7	98.5%	/
Yb	13.6 ± 1.2	/	13.6	102.5%	/
Lu	0.1 ± 0.03	/	0.1	101.8%	/

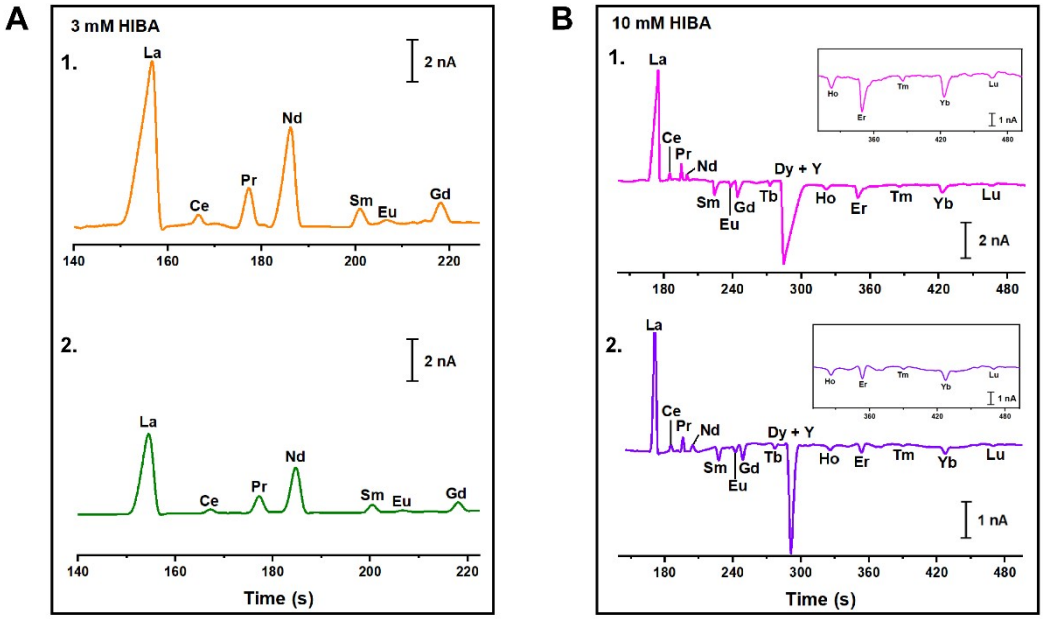

Figure S10. Electropherograms of the rare-earth mineral. A1 and B1 are the spiked samples; A2 and B2 are the samples. The inserts in (B) are the zoom-in views of electropherograms of Ho, Er, Tm, Yb and Lu. BGE: (A) 20 mM arginine (Arg) and 3 mM α-hydroxyisobutyric acid (HIBA) adjusted to pH 4.2 with acetic acid; (B) 20 mM Arg and 10 mM HIBA adjusted to pH 4.2 with acetic acid. Other test conditions are the same: Separation voltage: +16 kV. Cappillary: 50 μm ID, 365 μm OD, 20 cm separation length, 40 cm total length. Hydrodynamic injection: 30 s at 10 cm height. 1 MHz sine wave with an effective excitation voltage of 40 V_{pp}.

11. Definitions of S/N and linear range used in this work

Figure S11 shows the electropherogram of 50 nM Li^+, which has a peak height of 25 µV. The resolution of our system is less than 1 µV; the noise is less than 3 µV considering the short-term baseline drift. Calculated at a noise level of 3 µV, the S/N for 50 nM Li^+ is 8.3, and the 3 × S/N detection limit for Li^+ is calculated to be 20 nM, which is consistent with the experimental result. The lower limit of the linear range of the concentration response is 9 × S/N, that is, 60 nM.

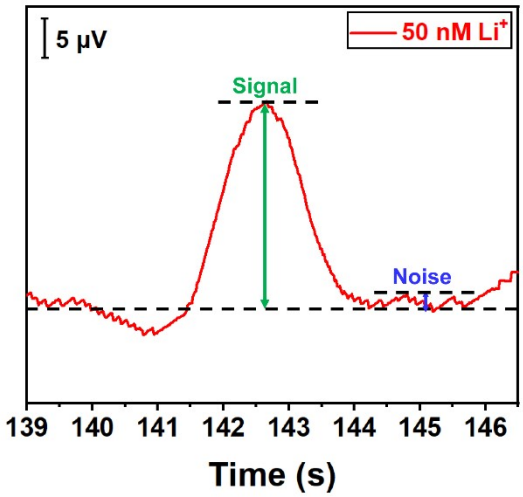

Figure S11. The definition of S/N used in this work, using 50 nM Li^+ as an example.

12. Performance evaluation of home-build and commercial CE-C^4D

Considering the difference in the design of the two instruments (e.g. eDAQ ER225 with 100 V_{pp}, but ours with 40 V_{pp}, a 2.5 times difference), we try our best to make them work under each other's optimal conditions. For a fair comparison, we conducted a comparative evaluation with both system operating under identical electrophoresis conditions, including same diameter capillary and injection condition. Specifically, for 75 µm ID capillary, the commercial CE-C^4D operates with differential detection at 800 kHz, 100 V_{pp} (Figure S12A), while our new CE-C^4D uses the "effective" differential detection with 1 MHz, 40 V_{pp} (Figure S12B). The comparative analysis revealed a significant reduction in noise by about 10 times and an overall performance is about 25 times with our CE-C^4D compared to the commercial CE-C^4D.

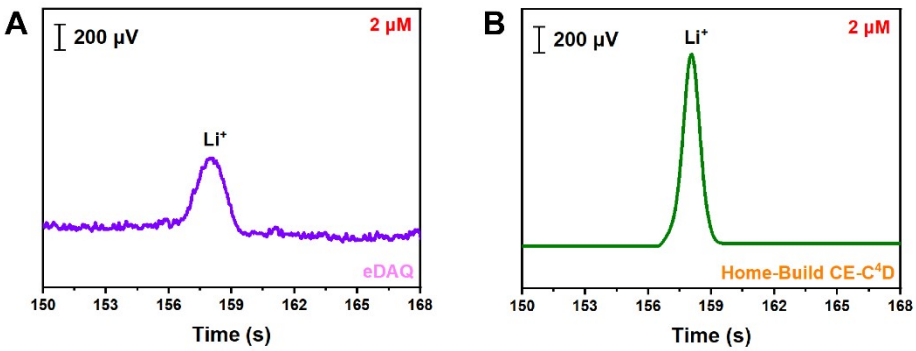

Figure S12. Performance evaluation of home-build and commercial CE-C^4D using 2 µM Li^+ as an example. BGE:

20 mM MES-His, pH = 6; capillary effective length: 20 cm, total length: 64 cm. (A) Commercial CE-C^4D (eDAQ, ER225 with ET120); differential detection; 800 kHz sine wave with effective excitation voltage of 100 V_{pp}. (B) Home-build CE-C^4D; "effective" differential detection; 1 MHz sine wave with an effective excitation voltage of 40 V_{pp}. Other electrophoretic conditions are the same: separation voltage: +15 kV; capillary with 75 μm ID and 365 μm OD; hydrostatic injection: 40 s at 10 cm height.

Reference

1. A. J. Zemann, E. Schnell, D. Volgger and G. K. Bonn, Analytical Chemistry, 1998, **70**, 563-567.
2. T. D. Mai, T. T. Pham, H. V. Pham, J. Saiz, C. G. Ruiz and P. C. Hauser, *Analytical Chemistry*, 2013, **85**, 2333-2339.
3. L. Zhang, S. S. Khaloo, P. Kubán and P. C. Hauser, *Measurement Science and Technology*, 2006, **17**, 3317-3322.
4. H. A. Duong, T. D. Nguyen, T. D. Mai, J. Sáiz and H. V. Pham, *Journal of Science: Advanced Materials and Devices*, 2016, **1**, 273-281.
5. K. J. M. Francisco and C. L. do Lago, *Electrophoresis*, 2009, **30**, 3458-3464.
6. M. Stojkovic, B. Schlensky and P. C. Hauser, *Electroanalysis*, 2013, **25**, 2645−2650.
7. M. C. Breadmore, *Journal of Chromatography A*, 2012, **1221**, 42−55.
8. W. Huang and P. K. Dasgupta, *Analytical Chemistry*, 2016, **88**, 12021−12027.
9. E. Baltussen, R. M. Guijt, G. van der Steen, F. Laugere, S. Baltussen and G. W. K. van Dedem, *Electrophoresis*, 2002, **23**, 2888−2893.
10. P. Tůma and J. Gojda, *Electrophoresis*, 2015, **36**, 1969−1975.
11. C. Wang, H. Xing, B. Zheng, H. Yuan and D. Xiao, *Scientific Reports*, 2020, **10**, 7944−7953.
12. T. Drevinskas, A. Maruska and V. Briedis, *Electrophoresis*, 2015, **36**, 292−297.
13. D. Shen, Y. Li, Z. Zhang, P. Zhang and Q. Kang, *Talanta*, 2013, **104**, 39−43.
14. M. Jaanus, A. Udal, V. Kukk, K. Umbleja, J. Gorbatsova and L. Molder, *Elektronika Ir Elektrotechnika*, 2016, **22**, 29−32.
15. H. Zheng, M. Li, J. Dai, Z. Wang, X. Li, H. Yuan and D. Xiao, *Analytical Chemistry*, 2014, **86**, 10065−10070.
16. T. Drevinskas, L. Telksnys, A. Maruska, J. Gorbatsova and M. Kaljurand, *Electrophoresis*, 2018, **39**, 2877−2883.
17. G. Fercher, A. Haller, W. Smetana and M. J. Vellekoop, *Analytical Chemistry*, 2010, **82**, 3270−3275.
18. E. Kratii, V. Nikonorov and T. Nikitina, *Microchemical Journal*, 2017, **130**, 198-204.